Science and Technology Journal Vol. 12 Issue: 2 June 2024 ISSN: 2321-3388

Ab initio Study of Halide Double Perovskite Cs_2NaAlX_6(X=Br,I) for Optoelectronics and Thermoelectric Materials

Teda H. Lalrinmawii[1*], Laihnuna[2], Z. Pachuau[3], Joel Lalbiakkima[4], and G.C. Lalremruata[5]

[1,2,3,4,5]Department of Physics, Mizoram University, Aizawl-796004, India

*E-Mail: zaiapach14@gmail.com

[*]Corresponding Author

Abstract—Halide double perovskites represent a diverse class of materials, allowing researchers to explore a wide range of properties and functionalities. This diversity opens up opportunities for innovation in various technological applications. They can exhibit tunable bandgaps by adjusting the composition of halide ions. We present a broad theoretical exploration of $Cs_2NaAl(Br/I)_6$, focusing on its prospect for advanced optoelectronic applications and thermoelectric devices. Utilizing computational simulations, we analyze the band structure, optical properties, and thermoelectric performance of this compound to determine its effectiveness in energy conversion. Cs_2NaAlI_6, exhibits a bandgap of 2.4 eV. Moreover, our calculations reveal a promising thermoelectric efficiency of 1.006 and 1.32 at room temperature for $Cs_2NaAl(Br/I)_6$, suggesting its viability for waste heat recovery and power generation.

Keywords: Dielectric function, Seebeck coefficient, Absorption coefficient, Grüneisen parameter

INTRODUCTION

Recent advances in material science have accelerated the search for novel materials with outstanding properties, particularly in optoelectronics and thermoelectrics. Halide double perovskites have garnered significant interest due to their exceptional structural flexibility, tunable electronic properties, and potential for high-performance applications (Jain *et al*. 2018). These materials, with the general formula $A_2BB'X_6$—where A is a monovalent cation, B and B′ are distinct metal cations, and X is a halide anion—offer a rich compositional space that facilitates precise property tuning (Jain *et al*. 2018). Specifically, Cs_2NaAlX_6 (X = Br, I) have emerged as promising candidates for both optoelectronic and thermoelectric applications, thanks to their favourable band gaps, high stability, and the ability to achieve high carrier mobility and low thermal conductivity (NREL, 2020; Zhao *et al*. 2016). The substitution of halide anions (Br, I) in these compounds provides additional flexibility to fine-tune their electronic and thermal properties, making them versatile for next-generation technologies (Zhao *et al.* 2016).

In this study, we employ ab initio methods to investigate the structural, electronic, optical, and thermoelectric properties of Cs_2NaAlX_6 (X = Br, I). Utilizing first-principles calculations, we aim to develop a thorough understanding of these materials' fundamental characteristics and explore their potential for use in optoelectronic devices, such as light-emitting diodes (LEDs) and solar cells, as well as in thermoelectric applications where efficient waste heat conversion is crucial. The insights gained from this research will contribute to the ongoing development of halide double perovskites as versatile and high-performance materials for modern technology (Blancon *et al*. 2020).

https://doi.org/10.22232/stj.2024.12.02.12

Halide double perovskites represent a diverse class of materials, allowing researchers to explore a wide range of properties and functionalities (Cai *et al*. 2019). This diversity opens up opportunities for innovation in various technological applications. Halide double perovskites offer several advantages in various technological applications, making them promising candidates for diverse fields. They can exhibit tunable bandgaps by adjusting the composition of halide ions. They can be employed in electronic devices, including transistors and integrated circuits, contributing to advancements in electronics. Halide double perovskites often have high absorption coefficients and tunable bandgap which makes them suitable for applications in optoelectronics, like photodetectors, solar cells and LEDs (Charef *et al*. 2024). Kong *et al*. effectively synthesized Cs_2TiCl_6 and Cs_2TiBr_6 at room temperature utilizing solution-based methods.The study finds that cesium titanium halide perovskites (Cs_2TiX_6) exhibit tunable band gaps (1.7-2.5 eV), stable photoluminescence (535-670 nm), and high thermal stability up to 500°C. These lead-free perovskites, synthesized via a scalable room-temperature process, are promising for eco-friendly optoelectronic applications (Kong *et al*. 2020). Ghrib *et al.* found that $K_2Ti(Cl/Br)_6$ double perovskites are stable with direct band gaps of 2.80 eV (K_2TiCl_6) and 2.1 eV (K_2TiBr_6). Their strong absorption in the visible to ultraviolet range (2.5-4 eV) makes them suitable for solar cell applications with static dielectric constants of 3.16 and 3.62 (Ghrib *et al*. 2021). Slavney *et al.* study explores $Cs_2AgBiBr_6$, a lead-free double perovskite incorporating nontoxic Bi^{3+}, as a potential solar cell material. It demonstrates a long photoluminescence lifetime of ~660 ns and an indirect bandgap of 1.95 eV, making it suitable for tandem solar cells (Slavney *et al*. 2016). Volonakis *et al*. introduces Cs_2InAgX_6(X = Cl, Br, I) as a new class of lead-free halide double perovskites with potential for photovoltaics. First-principles calculations predict these compounds have direct band gaps, with $Cs_2InAgCl_6$ exhibiting 3.3 eV band gap and reversible color change under UV light (Volonakis *et al*. 2017). Recent investigations on $Rb_2AgIn(Cl/Br/I)_6$, reveal their potential as lead-free alternatives in photovoltaics and thermoelectric devices. The study found direct band gaps of 2.62 eV ($Rb_2AgInCl_6$), 1.74 eV ($Rb_2AgInBr_6$), and 0.56 eV (Rb_2AgInI_6) at the Γ-point, with absorption edges at 2.48 eV, 1.67 eV, and 0.45 eV, respectively (Hnuna *et al*. 2023). Huma *et al*. finds that lead-free double perovskites A_2SnI_6 (A = Cs, Rb) are mechanically stable and ductile, with direct band gaps of 1.147 eV and 1.197 eV, respectively. They exhibit visible spectrum absorption and p-type semiconducting behavior, with stable thermoelectric performance across 200–800 K (Huma *et al*. 2021). Ali *et al*. evaluates the thermoelectric properties of $Tl_2(Se,Te)Cl_6$ vacancy-ordered double perovskites using BoltzTraP and Wien2k codes. Both compounds exhibit indirect band gaps (2.976 eV for Tl_2SeCl_6 and 3.037 eV for Tl_2TeCl_6), with high Seebeck coefficients (183.50 μVK^{-1} and 185.49 μVK^{-1}, respectively), indicating p-type conductivity (Ali *et al*. 2021). Murtaza *et al.* investigates $X_2AgTlCl_6$ (X = Rb,Cs) double perovskites, revealing their suitability for optoelectronic applications with band gaps of 0.78 eV ($Rb_2TlAgCl_6$) and 0.74 eV ($Cs_2TlAgCl_6$). Both compounds exhibit high figures of merit (0.72 and 0.68) at elevated temperatures, making them promising for thermoelectric (Murtaza *et al* 2021). Recent research has increasingly focused on lead-free double halide perovskites for energy applications, owing to their tunable properties achievable through the substitution of various halide ions and metal cations (Karim *et al*. 2019; Saeed *et al*. 2020; Kale *et al* 2021; Mahmood *et al*. 2021; Nabi *et al*. 2021; Kangsabanik *et al*. 2018; Chakraborty *et al*. 2017). $Cs_2NaAl(Br/I)_6$ belongs to HDP family, which exhibit intriguing electronic and optical properties emerging due to the combination of two distinct cations inhabiting the A-site. Furthermore, the substitution of halide ions provides additional degrees of freedom to tailor the bandgap and optoelectronic attribute of $Cs_2NaAl(Br/I)_6$. We provide a comprehensive overview study of $Cs_2NaAl(Br/I)_6$ and its feasibility for optoelectronic and thermoelectric device applications of this material.

In summary, our investigation into $Cs_2NaAl(Br/I)_6$ compounds has revealed key insights into their structural stability, electronic properties, and potential applications. The negative enthalpy of formation confirms their thermodynamic stability, making them viable for synthesis. Stability trends among the halides highlight the influence of halogen size and electronegativity on formation energy. Goldschmidt and Bartel tolerance factors further validate the stability of these compounds in the cubic phase. Band structure analysis shows direct bandgaps, with halogen substitution impacting electronic transitions and absorption spectra. The computed elastic constants indicate strong mechanical stability, meeting Born stability criteria, with some anisotropy. Dielectric function analysis ($\varepsilon_1(\omega)$ and $\varepsilon_2(\omega)$) reveals capacitive behaviour, polarization variations, and shifts in resonance due to halide changes. Refractive index data suggest a high ionic bond concentration and semiconductor-like transparency, with significant visible light absorption. Importantly, thermoelectric efficiencies of 1.006 and 1.32 at room temperature suggest $Cs_2NaAl(Br/I)_6$

as promising candidates for waste heat recovery and power generation. The study also shows that transitioning from $Cs_2NaAlBr_6$ to Cs_2NaAlI_6 increases specific heat, enhancing vibrational modes and anharmonicity. The negative ΔG indicates a spontaneous tendency toward a lower energy state, and a nearly constant Debye temperature highlights the materials' thermal conductivity and hardness.

COMPUTATIONAL DETAILS

The calculations were performed using Density Functional Theory (DFT) with the FP-LAPW method in the WIEN2k software (Blaha *et al*. 2001). For analyzing band gaps and optical properties, the modified Becke-Johnson (mBJ) exchange-correlation potential was employed (Tran *et al*. 2009). The basis set was optimized with a product of R_{MT} and *k*max set to 8, and *l*max to 10, where *k*max is the maximum wave vector and R_{MT} is the smallest muffin-tin radius. The Fourier charge density was set to 12 Ry, with an energy threshold of −6.0 Ry, and 5000 k-points were utilized. Convergence criteria were set at 0.0001 Ry for energy and 0.001 e for charge (Hnuna *et al*. 2023). Thermoelectric properties were evaluated using semi-classical Boltzmann transport theory with a constant relaxation time approximation, as implemented in BoltzTraP2 (Madsen *et al*. 2018). Thermodynamic properties were obtained through the quasi-harmonic Debye model using the GIBBS2 code (de-la-Roza *et al*. 2011). Elastic constants were computed using the IRelast package, integrated with WIEN2k and specifically customized for cubic systems (Jamal *et al*. 2018).

RESULTS AND DISCUSSION

Structural and Electronic Properties

The image shows the optimized crystal structures of two halide double perovskites: $Cs_2NaAlBr_6$ on the left and Cs_2NaAlI_6 on the right. Both structures are depicted in a cubic phase, which is typical for this class of materials. The computed ground state properties of $Cs_2NaAl(Br/I)_6$ is shown in Table 1. Thermodynamics stability can be tested on the exothermic nature of the synthesis reaction, which can be calculated by the enthalpy of formation (ΔH_f). A negative ΔH_f indicates an exothermic reaction, signifying material stability. The formation enthalpy for $Cs_2NaAl(Br/I)_6$ was determined by (Hnuna *et al*. 2023);

$$\Delta H_f = E_{tot} - \left[mE_K + E_{In} + E_{Ag} + nE_x\right] \quad (1)$$

Here, E_{tot} represents the total energy of $Cs_2NaAl(Br/I)_6$, while E_{Cs}, E_{Na}, E_{Al}, and E_x denote the energies of Cs, Na, Al, and Br/I, respectively. The determined ΔH_f is provided in Table 1. The negative ΔH_f indicates the thermodynamic stability of $Cs_2NaAl(Br/I)_6$ (Zelai *et al*. 2024). The decrease in electronegativity from chlorine to iodine contributes to the increase in enthalpy of formation. To assess the cubic phase stability of $Cs_2NaAl(Br/I)_6$, we computed the Goldschmidt tolerance factor (t_G) and the octahedral factor (μ) using the provided equation (Hnuna *et al*. 2023; Goldschmidt 1926)

$$t_G = \frac{r_A + r_X}{\sqrt{2}\,(\bar{r}_B + r_X)} \quad (2)$$

$$\mu = \frac{\bar{r}_B}{r_X} \quad (3)$$

Here, r_A represents the ionic radius of Cs, $\bar{r}_B$ is the average of the ionic radii of Na and Al, and r_X denotes the ionic radius of the halides Br, and I. Nevertheless, current research indicates that the precision of the Goldschmidt tolerance (t_G) is frequently inadequate (Bartel *et al*. 2019). Using the newly introduced model by Bartel *et al*. (Hnuna *et al*. 2023), we calculated the tolerance factor to prevail over the drawbacks of the Goldschmidt tolerance factor (τ_B) (Bartel *et al*. 2019). The updated tolerance factor, τ_B is given as:

$$\tau_B = \frac{r_X}{\bar{r}_B} - n_A\left[n_A - \frac{r_A/\bar{r}_B}{\ln(r_A/\bar{r}_B)}\right] \quad (4)$$

For a stable cubic phase, τ_B needs to be less than 4.18 (Bartel *et al*. 2019), and the values of t_G should lie in the ranges of 0.9 to 1.02 and μ should fall within the ranges of 0.41 to 0.73 (Li *et al*. 2008). The calculated values of t_G, μ, and τ_B for $Cs_2NaAl(Br/I)_6$ are shown in Table 1, indicating their stability in the cubic phase.

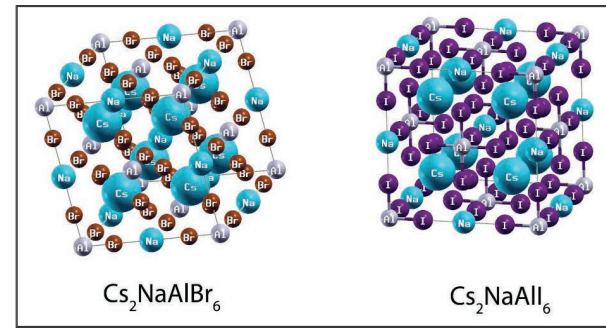

Fig. 1: Crystal Structure of $Cs_2NaAl(Br/I)_6$.

We utilized high-symmetry points within the BZ to compute the energy band of $Cs_2NaAl(Br/I)_6$. Fixing E_F at zero, we identified the maximum valence band (VB) and minimal conduction band (CB) at the Γ-points in the BZ, indicating direct bandgaps for $Cs_2NaAl(Br/I)_6$. Larger halogen atoms

with more diffuse atomic orbitals were produced when halogen ions were switched from Br to I. Consequently, increased overlap between the atomic orbitals of cations and anions weakened bonding and extended the electron cloud, leading to smaller energy gaps. The bandgap serves as the lower threshold for absorption, with $Cs_2NaAlBr_6$ and Cs_2NaAlI_6 exhibiting absorption within the ultraviolet spectrum. This suggests plausible applications of $Cs_2NaAl(Br/I)_6$ in optoelectronic devices operating within these spectral range. Table 1 displays the band gap values that were computed.

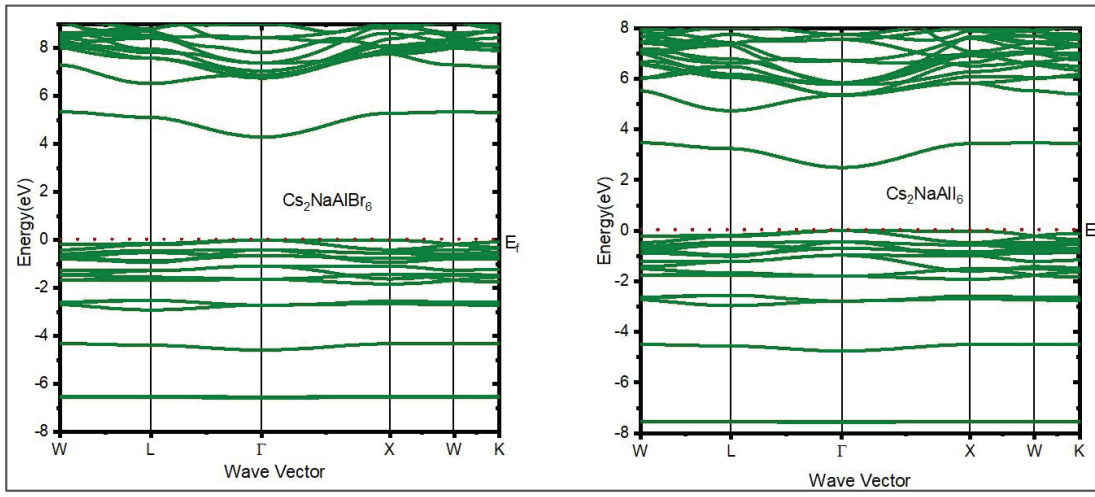

Fig. 2: Calculated Band Structures of $Cs_2NaAl(Br/I)_6$.

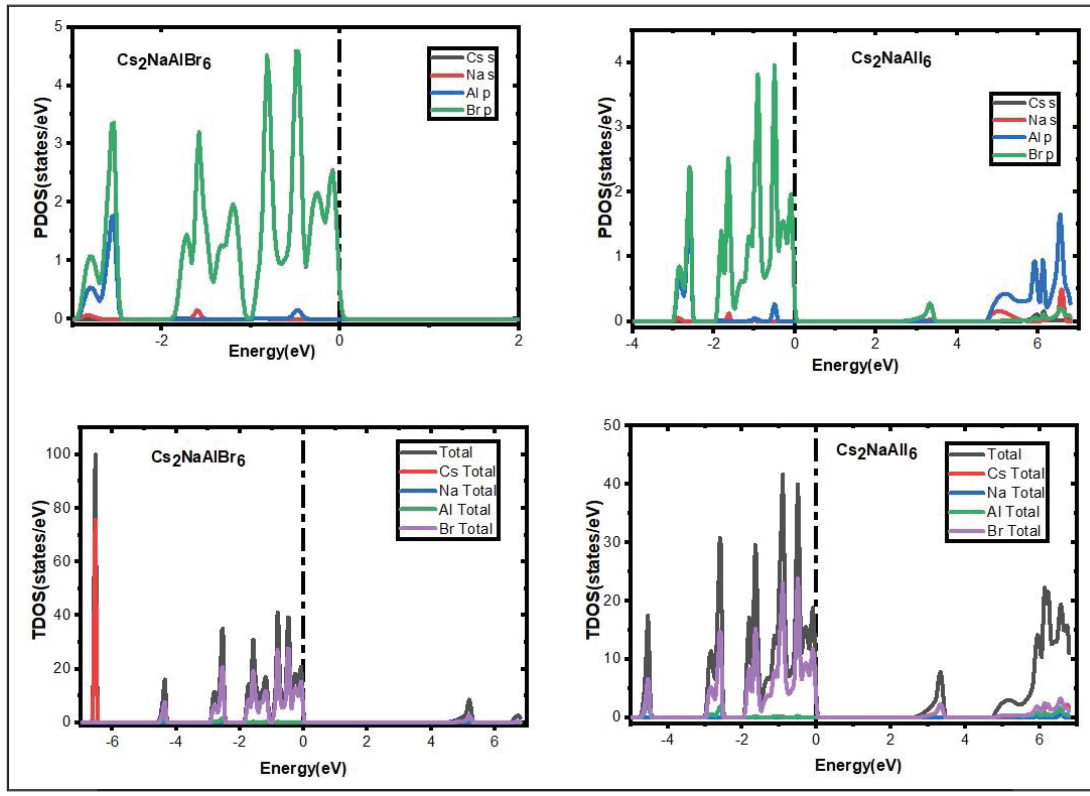

Fig. 3: Calculated Partial and Total Density of States of $Cs_2NaAl(Br/I)_6$.

Table 1: Computed Ground State Properties of $Cs_2NaAlBr_6$ and $Cs_2NaAlBr_6$.

Parameters	$Cs_2NaAlBr_6$	Cs_2NaAlI_6
a(Å)	11.1595	12.1766
V_o(Bohr^3)	2344.6043	3045.8909
E_o(Ry)	-63252.509176	-117401.213800
B(GPa)	21.7419	15.9015
B'	3.4210	3.9728
E_g(eV)	4.290	2.493
$\triangle H_f(eV)$	-1.969	-1.408
τ_G	0.90	0.96
μ	0.5659	0.4381
τ_B	3.884	4.07

To enhance our understanding of the energy band structure, we computed the partial density of states (PDOS) and the total density of states (TDOS), as shown in Figure 3. The TDOS offers a detailed overview of the material's energy band, illustrating how the energy levels are distributed. Peaks and variations in the TDOS correspond to specific electronic transitions. Notably, the energy band derived from energy-dispersed states align with the TDOS, confirming their consistency. Additionally, the energy band structure obtained from the energy-dispersed states aligns with the TDOS, confirming their consistency. The PDOS provides a more detailed analysis, revealing the contributions of individual orbitals to the electronic states (Nabi *et al*. 2021).

Mechanical Properties

Table 2 displays the calculated elastic constants and their corresponding mechanical properties, offering important insights into the material's mechanical behavior (Ziane *et al* 2014).

Table 2: Calculated Elastic Constant and Derived Mechanical Parameters.

Parameters	$Cs_2NaAlBr_6$	Cs_2NaAlI_6
C_{11} (GPa)	39.783	23.957
C_{12} (GPa)	14.192	13.177
C_{44} (GPa)	13.441	9.523
G_V (GPa)	13.183	7.870
G_R (GPa)	13.175	7.288
G (GPa)	13.179	7.579
B (GPa)	22.723	16.770
B/G	1.724	2.213
Y (GPa)	33.140	20.416
υ	0.257	0.297
A	1.0205	1.319
C′	12.796	5.39
C′′	0.751	3.654
A^G	0.0304	3.840
A^U	0.00304	0.39928
θ_D (K)	188.806	129.305
V_l (m/s)	3257.504	2609.127
V_t (m/s)	1862.957	1385.540
V_m (m/s)	2069.937	1548.330

For mechanical stability, the Born stability conditions must be fulfilled [30], i.e.,

$$(C_{11} + 2C_{12}) > 0; C_{11} - C_{12} > 0; C_{44} > 0 \quad (5)$$

Based on the calculated elastic constants, $Cs_2NaAl(Br/I)_6$ demonstrates mechanical stability as it satisfies the Born mechanical stability conditions outlined in Equation 5. B/G ratio was employed for assessing the ductility or brittleness, revealing values of 1.724, signifying brittle behavior for $Cs_2NaAlBr_6$ and 2.213 for Cs_2NaAlI_6 which shows ductile behaviour . The Poisson's ratio (ν), falls within the range of $0 < \nu < 0.5$ (Draxl *et al* 2006), suggesting limited plasticity in these halide double perovskites compounds. Different levels of anisotropy were found across the series by computing the elastic anisotropy percentages (A^G) and the universal elastic anisotropy index (A^U).

This analysis, summarized in Table 2. Using the ELATE software (Gaillac *et al*. 2016), we generated three-dimensional (3D) representations depicting the directional dependence of Young's modulus (Y), linear compressibility (β), shear modulus (G), and Poisson's ratio (υ) for $Cs_2NaAl(Br/I)_6$. The level of anisotropy is visually represented by deviations from spherical shapes in the figures, reflecting variations in physical attributes across different orientations (Aravindan *et al*. 2022). Table 3 summarizes the maximum and minimum values for these properties obtained for $Cs_2NaAl(Br/I)_6$.

Table 3: The Values of Young's Modulus (Y), Linear Compressibility (β), Shear Modulus (G), and Poisson's Ratio (υ) (Hnuna *et al*. 2023), at their Maximum and Minimum are.

Compound	Y (GPa)		β (TPa-1)		G (GPa)		υ	
	Y_{Min}	Y_{Max}	β_{Min}	β_{Max}	G_{Min}	G_{Max}	υ_{Min}	υ_{Max}
$Cs_2NaAlBr_6$	32.32	33.682	14.67	14.67	12.796	13.441	0.23989	0.27116
Cs_2NaAlI_6	14.605	24.022	19.876	19.876	5.39	9.523	0.086185	0.50262

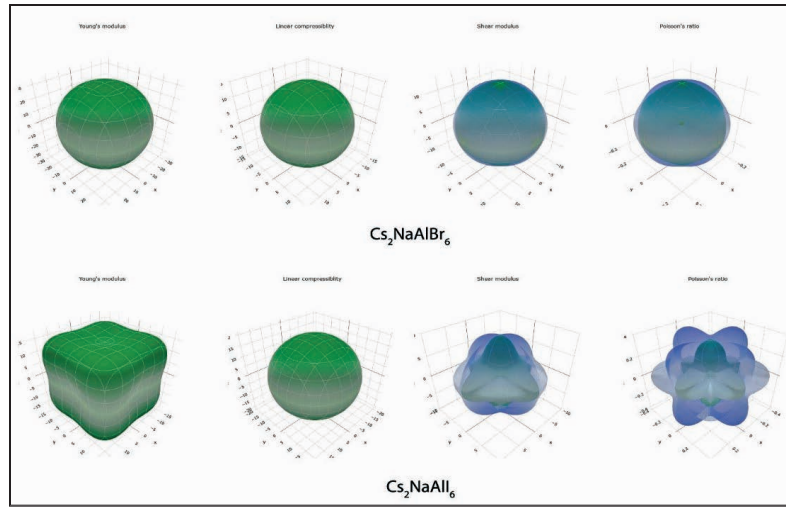

Fig. 4: Three-dimensional Graphical Representation of Young's Modulus, Linear Compressibility, Shear Modulus, and Poisson's Ratio of $Cs_2NaAl(Br/I)_6$.

Optical Properties

The linear response of a solid's macroscopic optical properties is generally characterized by the complex dielectric function, which can be computed by the following equation (Kramers, 1927, Kronig 1926):

$$\varepsilon(\omega) = \varepsilon_1(\omega) + i\varepsilon_2(\omega) \quad (6)$$

The extent of a material's polarization under incident light at the plasmonic resonance frequency is represented by $\varepsilon_1(\omega)$ while $\varepsilon_2(\omega)$ describes the level of light absorption by the material (Draxl, 2006). The imaginary component of the dielectric function, $\varepsilon_1(\omega)$, can be determined using the relevant momentum matrix, as shown below (Penn, 1962):

$$\varepsilon_2(\omega) = \frac{e\hbar}{\pi m^2\omega^2}\sum_{\upsilon,c}\int |M_{c\upsilon}(k)|^2\,\delta\,[\omega_{c\upsilon}(k)-\omega]d^3k \quad (7)$$

The Kramer-Kronig transformation can be used to get $\varepsilon_1(\omega)$ from $\varepsilon_2(\omega)$ (Khandy *et al*. 2016) as,

$$\varepsilon_1(\omega) = 1 + \frac{2}{\pi}P\int_0^\infty \frac{\omega'\varepsilon_2(\omega')}{\omega'^2-\omega^2}d\omega' \quad (8)$$

The following equations can be employed to determine distinct optical properties, including reflectivity (Ziane *et al*. 2014), refractive index, extinction coefficient (Cheddadi *et al*. 2017), and absorption coefficient (α) (Ziane *et al*. 2014).

$$R(\omega) = \left|\frac{\varepsilon^{\frac{1}{2}}(\omega)-1}{\varepsilon^{\frac{1}{2}}(\omega)+1}\right| \quad (9)$$

$$\alpha(\omega) = \sqrt{2}\omega\left[\left(\sqrt{\varepsilon_1^2(\omega)+\varepsilon_2^2(\omega)}\right)-\varepsilon_1(\omega)\right]^{\frac{1}{2}} \quad (10)$$

$$n(\omega) = \left[\frac{\varepsilon_1}{2}+\frac{\sqrt{\varepsilon_1^2(\omega)+\varepsilon_2^2(\omega)}}{2}\right]^{\frac{1}{2}} \quad (11)$$

$$k(\omega) = \left[\frac{\sqrt{\varepsilon_1^2(\omega)+\varepsilon_2^2(\omega)}}{2}-\frac{\varepsilon_1}{2}\right]^{\frac{1}{2}} \quad (12)$$

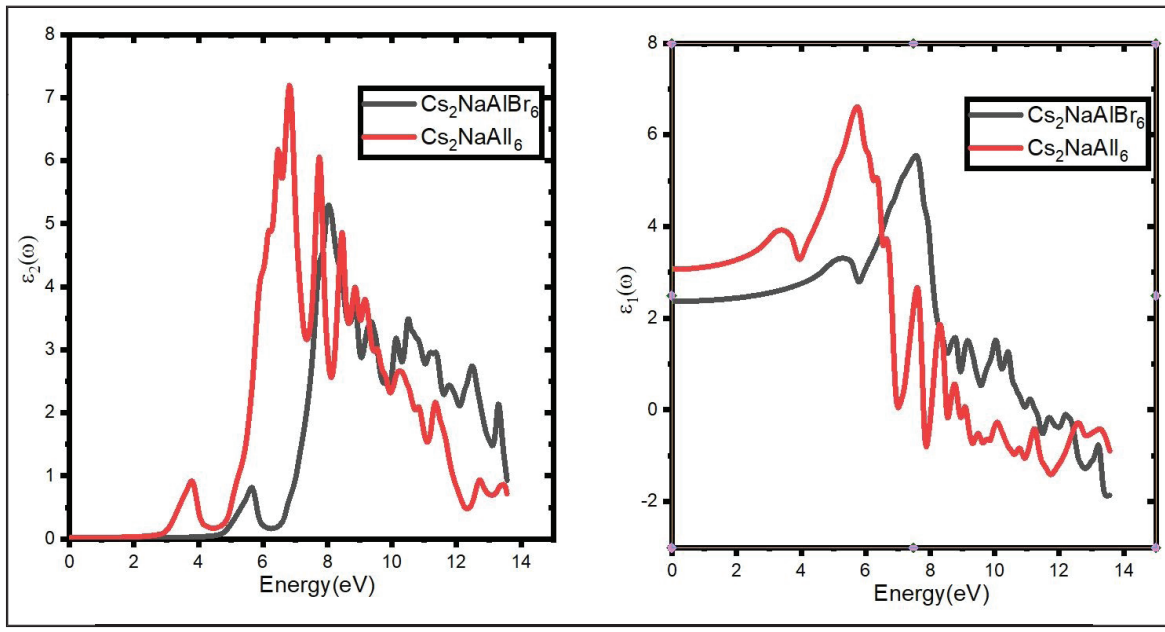

Fig. 5: Calculated (a) Imaginary and (b) Real Parts of Dielectric Function of $Cs_2NaAl(Br/I)_6$.

Figure 5 (b) illustrates the computed $\varepsilon_1(\omega)$ for $Cs_2NaAl(Br/I)_6$. $\varepsilon_1(\omega)$ signifies the material's capacity to retain and release electrical energy through polarization in response to an external electric field, indicating its capacitive behavior. Notably, the peak polarization occurs at 7.55 eV for $Cs_2NaAlBr_6$ and at 5.75 eV for Cs_2NaAlI_6. The change in resonance point towards lower energies with changing halides from Br to I is credited to the lowering of the energy gap (Kramers, 1927). Larger halogen ions possess increased polarizability due to their higher electron count, contributing to a higher real part of the dielectric constant. Consequently, heavier halogen ions exhibit stronger ionic polarization, resulting in enhanced capacitive behavior. The negative $\varepsilon_1(\omega)$ in the UV region indicates high absorption and polarization disappearance. The inverse correlation between the static dielectric constant and the band gap focus on the defect-tolerance capabilities of the compounds (Penn, 1962). Higher dielectric constants imply stronger Coulombic screening, reducing defect carrier-capture cross-sections and suppressing non-radiative recombination rates. Table 4 lists the calculated $\varepsilon(0)$ values of $Cs_2NaAl(Br/I)_6$. Figure 5 (a) showcases the calculated $\varepsilon_2(\omega)$ for $Cs_2NaAl(Br/I)_6$, revealing the frequency at which the material experiences maximum absorption of electromagnetic energy. The peak position in $\varepsilon_2(\omega)$ is indicative of loss mechanisms within the material, including absorption and dissipation of energy. Notably, as we transition from Bromine to Iodine, the size of the halogen atoms increases. Larger atoms exhibit lower-frequency vibrations, contributing to a downward shift in the peak value position. The fundamental edge of absorption, occurring at 4.86 eV, and 2.97 eV for $Cs_2NaAl(Br/I)_6$ corresponds to direct transitions between the lowest conduction band and highest valence band. As the size of the halogen atoms increases, ionization energies decrease, leading to lower-energy electronic transitions. Consequently, the fundamental edge of absorption tends to decrease with larger halogen atoms. The maximum intensity of these peaks, occurring at 7.83 eV, and 6.47 eV for $Cs_2NaAl(Br/I)_6$ respectively, highlights the zone of highest absorption within the ultraviolet spectrum. Notably, the magnitude of $\varepsilon_2(\omega)$ peaks increases and shifts towards decreased energies with alterations in halides from Bromine to Iodine, attributed to the expansion of the electron cloud from Bromine to Iodine.

Table 4: Computed Static Dielectric Constant $\varepsilon(0)$, Static Refractive Index $n(0)$ and Static Reflectivity $R(0)$.

Compound	$\varepsilon(0)$	$n(0)$	$R(0)$
$Cs_2NaAlBr_6$	2.37	1.54	0.0450
Cs_2NaAlI_6	3.07	1.75	0.0746

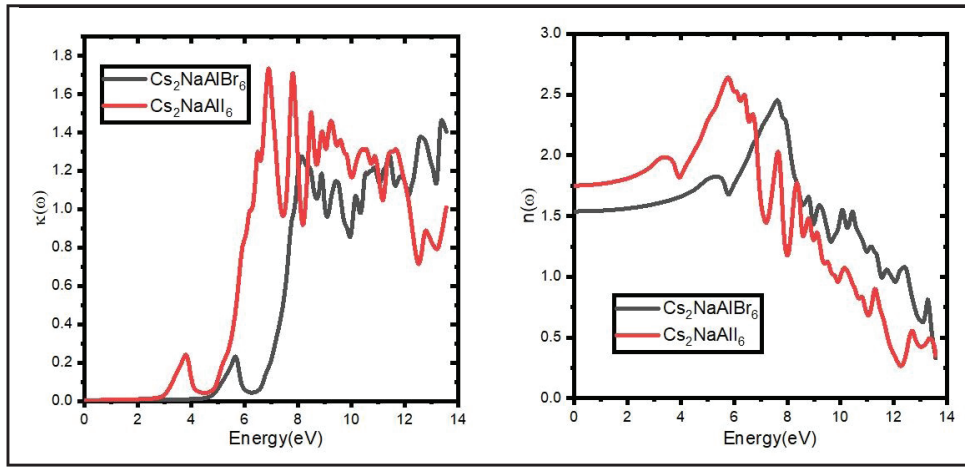

Fig. 6: Calculated (a) Extinction Coefficient and (b) Refractive Index of $Cs_2NaAl(Br/I)_6$.

Figure 6 (b) presents the calculated refractive index for $Cs_2NaAl(Br/I)_6$, offering insights into the type of interactions occurring when a photon interacts with the lattice. The refractive index reveals the nature of bonding in materials (Khandy *et al*. 2016). Covalently bonded materials generally exhibit higher n(ω) values compared to ionic compounds. This is because the stronger interactions between their shared electrons and incoming photons lead to a reduction in photon energy (Volonakis *et al*. 2017). Hence, materials with higher refractive indices typically feature more prominent covalent bonds, whereas those with lower refractive indices are characterized by predominant ionic bonds (Huma *et al*. 2021). The low refractive index observed in $Cs_2NaAl(Br/I)_6$ indicates the prevalence of ionic bonds within the compound. The transparency of a material is correlated with its refractive index, with semiconductors typically exhibiting values between 2–3 (Noor *et al*. 2018). The refractive index n(ω) rises in the IR and visible regions, reaching peaks at 7.86 eV and 5.93 eV in the UV region, before rapidly decreasing at elevated energies.At higher energies, the refractive index becomes fractional, transitioning the material's response towards a more metal-like behaviour, where group velocity exceeds phase velocity (Zai *et al*. 2003, Zhang *et al*. 2015). In Figure 6 (a), the calculated k(ω) for $Cs_2NaAl(Br/I)_6$ is depicted. The threshold energies of k(ω) begin at 4.72 eV, and 2.91 eV for $Cs_2NaAl(Br/I)_6$, closely aligned with the calculated bandgap. With energy in the visible range, these k(ω) values show a rising trend that peaks in the UV region. The computed $n(0)$ are summarized in Table 4.

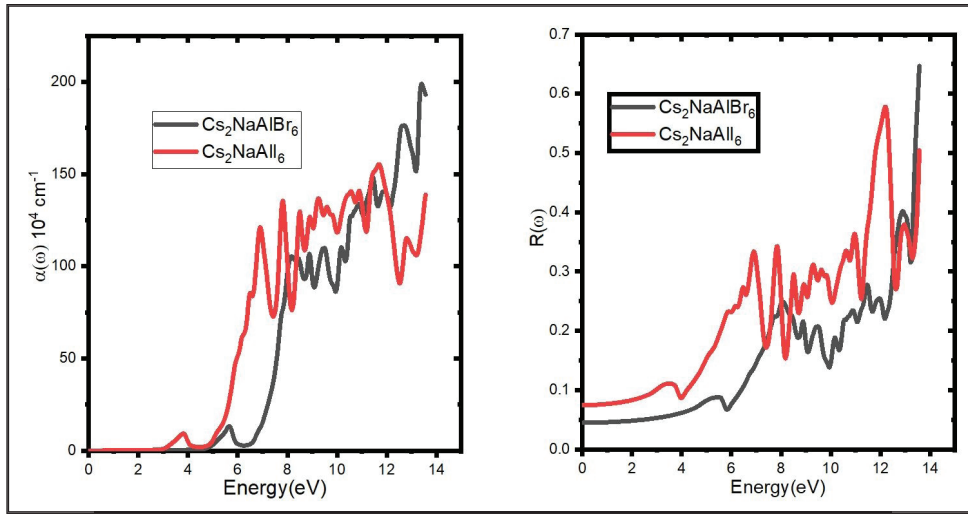

Fig. 7: Calculated (a) Absorption Coefficient and (b) Reflectivity of $Cs_2NaAl(Br/I)_6$.

In Figure 7 (a), the calculated α(ω) for $Cs_2NaAl(Br/I)_6$ are depicted. α(ω) displays two discernible categories of peaks: a shoulder peak ascribed to sub-bands and a noticeable peak coming from VB and CB transitions. Interestingly, the visible spectrum shows significant absorption in the first band of α(ω), with the UV area showing the highest absorption. R(ω) exhibit pronounced peaks in the ultraviolet spectrum, ranging from 7 to 14 eV, as displayed in Figure 7 (b). This suggests the promising potential of $Cs_2NaAl(Br/I)_6$, for applications in UV detectors, Bragg reflectors etc. Figure 7(b) illustrates a notable decrease in optical reflectivity within the low-energy range up to 6 eV, followed by a sharp increase in reflectivity at higher energy levels, with peaks observed beyond 11 eV for these compounds. The static reflectivity values that were computed are presented in Table 4. For $Cs_2NaAlBr_6$ and Cs_2NaAlI_6, the maximum reflectivity is 0.57 and 0.65, respectively, underscoring their effectiveness in the low-energy range. The low reflectivity scores, particularly evident in the visible and infrared regions, suggest transparency in these spectral regions, making these compounds suitable candidates for anti-reflective coatings.

Thermoelectric Properties

The thermoelectric properties of $Cs_2NaAl(Br/I)_6$ were calculated using semi-classical Boltzmann transport theory within the constant relaxation time approximation (RTA), as implemented in BoltzTraP2 (Madsen *et al*. 2018).

Figure 8(b) illustrates the computed electrical conductivity of the studied compounds. As temperature rises, the conductivity (σ) also increases, due to the enhanced ease with which carriers transition from the valence band to the conduction band at elevated temperatures. This observed rise in σ affirms the semiconducting behaviour of these materials. Notably, a decrease in σ is noted as Bromine is substituted with iodine. This decrease might be attributed to the growth of atoms, which leads to electron Coulomb repulsion and, as a result, limits carrier mobility. Additionally, the higher σ indicates a decrease in electrical resistivity (ρ = 1/σ) for the HDP.

Figure 8(a) presents the Seebeck coefficient (S), which quantifies the voltage shift caused by temperature variations (S = ΔV/ΔT) (Noor *et al*. 2018). The Seebeck coefficient is influenced by the carrier concentration and the effective mass associated with the density of states (DOS) (Yousuf *et al*. 2017), as shown below

$$S = \left[\left(\frac{8\pi^2}{3e}\right)\left(\frac{k_b^2}{h^2}\right)\left(\frac{3n}{\pi}\right)^{-2/3} m^*_{DOS}\, T\right] \quad (13)$$

Near the fermi level, materials with flat bands have a high effective mass and make good thermoelectric technology prospects. A positive Seebeck coefficient (S) indicates the presence of p-type carriers (Tang *et al*. 2011). The Seebeck coefficient exhibits an increasing trend with rising temperature. Additionally, Figure 8(a) highlights that Cs_2NaAlI_6 exhibits a higher Seebeck coefficient, which decreases when Iodine is replaced with Bromine. The decrease in the Seebeck coefficient is due to thermal agitation, which hinders carrier mobility and elevates the potential difference (Hnuna *et al*. 2023). The remarkable Seebeck coefficients observed in these HDPs can be attributed to the nearly flat conduction bands between the L and Γ directions, as shown in Figure 2. Table 5 lists the thermoelectric coefficients at room temperature.

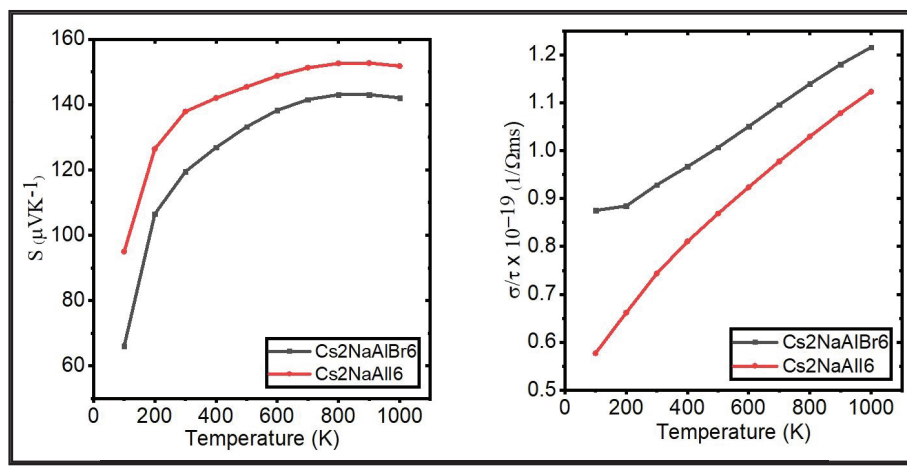

Fig. 8. Calculated (a) Seebeck Coefficient and (b) Electrical Conductivity of $Cs_2NaAl(Br/I)_6$.

Table 5: Computed Thermoelectric Coefficient at Room Temperature.

Compound	S (μVK^{-1})	σ (Ωm)$^{-1}$	κ_e (Wm^{-1}K^{-1})	*ZT*
$Cs_2NaAlBr_6$	119.503	9.29 x 10^{18}	3.95 x 10^{13}	1.006
Cs_2NaAlI_6	137.847	7.44 x 10^{18}	3.20 x 10^{13}	1.32

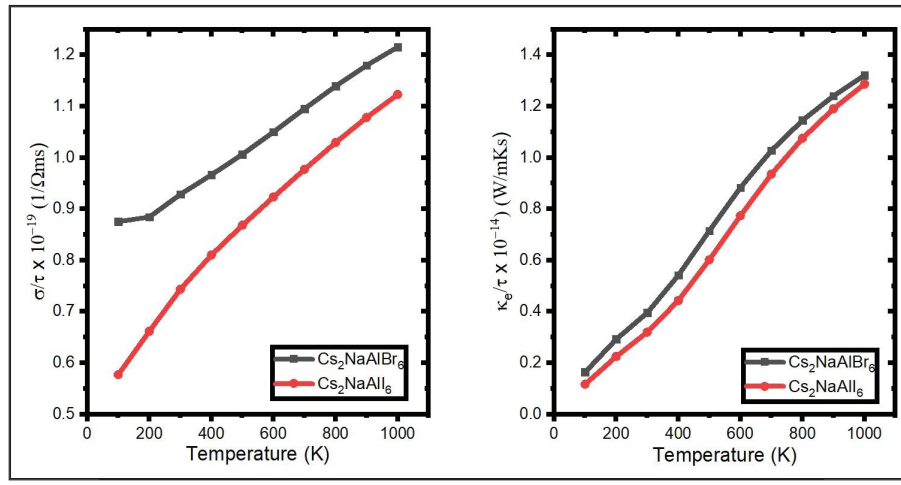

Fig. 9: Calculated Electrical and Thermal Conductivity of $Cs_2NaAl(Br/I)_6$.

Thermal conductivity arises from both electronic and lattice vibrations, which together constitute the overall thermal (Hnuna *et al.* 2023). Figure 9 illustrates the calculated electrical and thermal conductivities. The Wiedemann-Franz law, which relates electrical conductivity to thermal conductivity, is expressed as LT = κ/σ (Takeuchi, 2009). For ideal thermoelectric materials, maintaining a low ratio is crucial. $Cs_2NaAl(Br/I)_6$ exhibited exceptionally low κ/σ ratios, approximately on the order of 10^{-5}, making them highly suitable for thermoelectric applications.

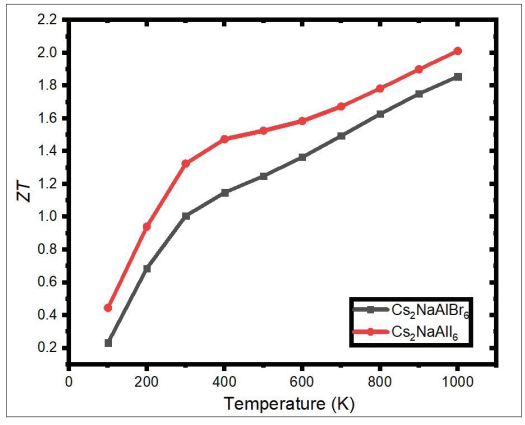

Fig. 10: Calculated Figure of Merit of $Cs_2NaAl(Br/I)_6$.

The efficiency of the thermoelectric material was estimated using the dimensionless figure of merit $ZT = S^2\sigma T/\kappa$ (Hnuna *et al.* 2023, Tritt *et al.* 2005). Figure 10 shows the temperature-dependent variation of *ZT*, with *ZT* increasing as the temperature rises.The combination of modest κ and large Seebeck S and σ is responsible for this increase in ZT. The efficiency of the materials elevated on substitution of halides from, Bromine to Iodine, owing to the augmented potential gradient.

Thermodynamic Properties

The thermodynamic properties were calculated using the GIBBS2 code in conjunction with the quasiharmonic Debye model (de-la-Roza *et al.* 2011). Figure 11 shows the specific heat values at constant pressure and constant volume obtained from these calculations. Specific heat at constant pressure and volume is a key thermodynamic property that indicates the amount of energy required to increase the temperature of a substance by one degree Celsius or Kelvin while keeping pressure or volume constant, respectively (Pan *et al.* 2016). Transitioning from $Cs_2NaAlBr_6$ to Cs_2NaAlI_6 involves a larger halogen atom size (Br, I), leading to reduced vibrational frequencies within the crystal lattice. This

augmented vibrational motion translates to higher heat capacity, as more energy is required to stimulate these modes. Under 400 K, the C_V values exhibit temperature sensitivity, increasing quickly and having a somewhat steep slope in accordance with Debye's T^3 law. This is mainly due to the exponential rise in the number of excited phonon modes (Pan *et al*. 2016), with long-wavelength lattice vibrations being the primary contributors to the heat capacity at constant volume.The values of C_V approach a constant at temperatures above 400 K, in accordance with the Dulong-Petit law (Hadi *et al*. 2017).

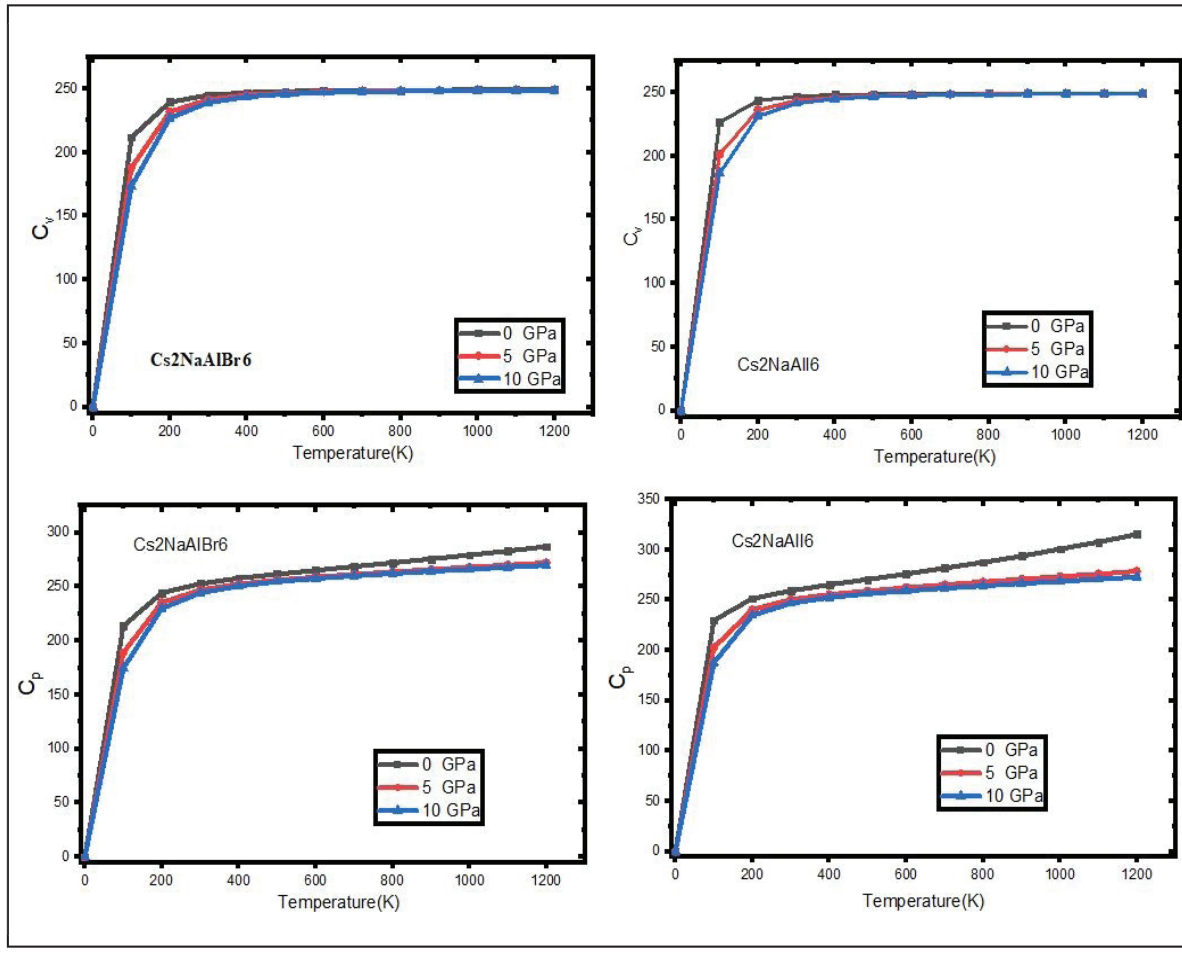

Fig. 11: Calculated Specific Heat at Constant Volume and Pressure of $Cs_2NaAl(Br/I)_6$.

The calculated Gibbs free energy (G) and entropy (S) are illustrated in Figure 12. G, a thermodynamic potential, amalgamates enthalpy and entropy, offering insights into the spontaneity and thermodynamic favourability of a process. It acts as an indicator of the maximum work that can be extracted from a system under constant temperature and pressure conditions (Hadi *et al*. 2017). A negative ΔG denotes a spontaneous process, indicating the system's tendency towards a lower energy state. Conversely, a positive ΔG suggests a non-spontaneous process necessitating input work. Entropy (S), in contrast, represents the level of disorder or randomness within a system, which is crucial for understanding the physical properties of materials. The entropy change (ΔS) delineates the system's disorder, with a positive ΔS favouring spontaneity by indicating an increase in system disorder. As the size of halogen atoms progresses from Bromine to iodine, larger atoms exhibit lower vibrational frequencies, intensifying vibrational modes and augmenting entropy. Larger atoms offer increased options for atomic arrangement, resulting in a greater number of microstates and consequently higher entropy.

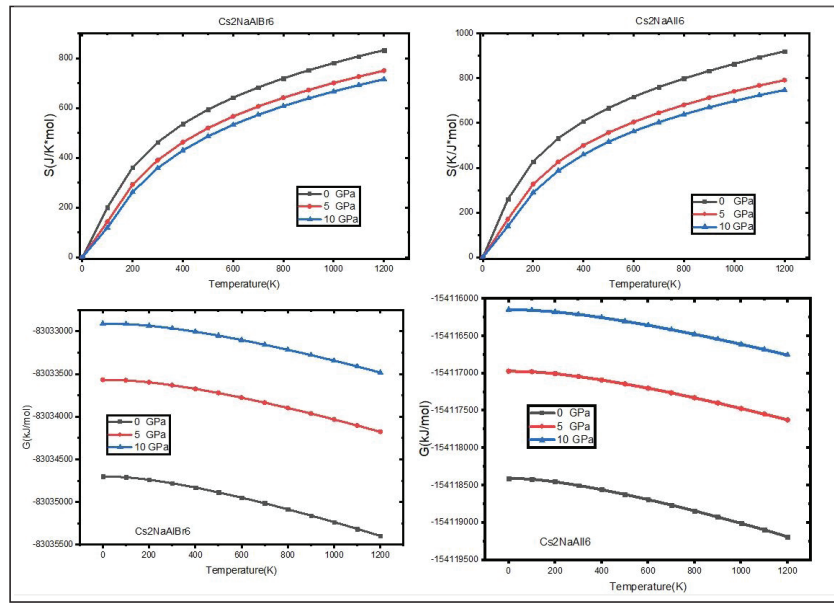

Fig. 12: Calculated Entropy and Gibb's Free Energy of $Cs_2NaAl(Br/I)_6$.

Figure 13 (b) illustrates the computed thermal expansion coefficient (α). This coefficient quantifies the fractional change in size for each Kelvin rise in temperature, offering insights into a material's expansion or contraction behaviour. A positive α denotes expansion, while a negative value signifies contraction, shedding light on the material's thermal responsiveness. The positive thermal expansion coefficients observed across the entire temperature spectrum for $Cs_2NaAl(Br/I)_6$ indicate their propensity to expand with increasing temperature. A higher thermal coefficient implies greater sensitivity to temperature variations, where even minor temperature fluctuations can induce notable dimensional changes. Understanding thermal expansion coefficients is crucial in engineering applications, particularly in structural design, where maintaining dimensional stability is paramount.

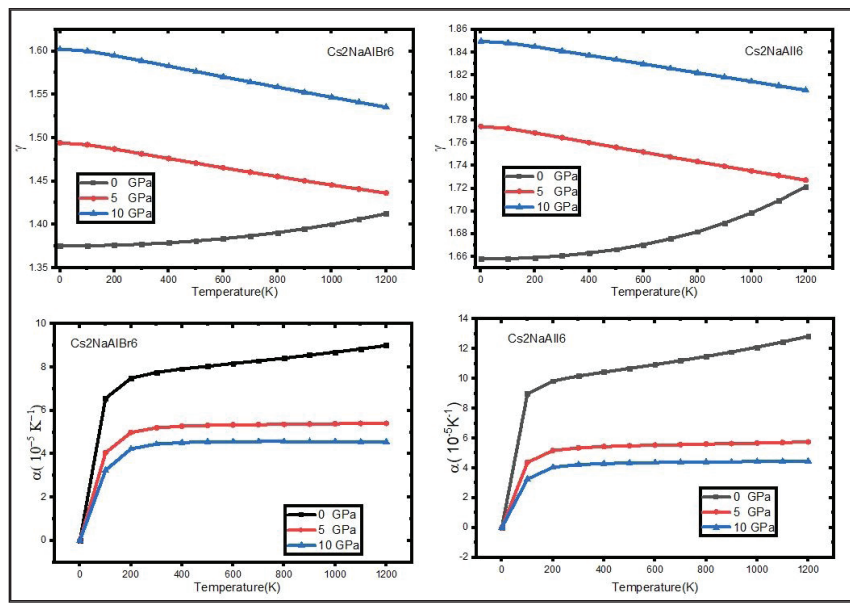

Fig. 13: Calculated Grüneisen Parameter and Thermal Expansion Coefficient of $Cs_2NaAl(Br/I)_6$.

In Figure 13 (a), the computed Grüneisen parameter (γ) is presented. While a harmonic crystal exhibits solely harmonic oscillations, real materials feature notable anharmonic effects, quantified by the Grüneisen parameter. The observed trend in γ for $Cs_2NaAl(Br/I)_6$ reveals a decrease as Bromine is replaced with Iodine. This variation correlates with the increasing size of halogen atoms within the group. Larger atoms possess greater degrees of freedom and tend to exhibit softer vibrational modes, influencing the overall anharmonicity of lattice vibrations.

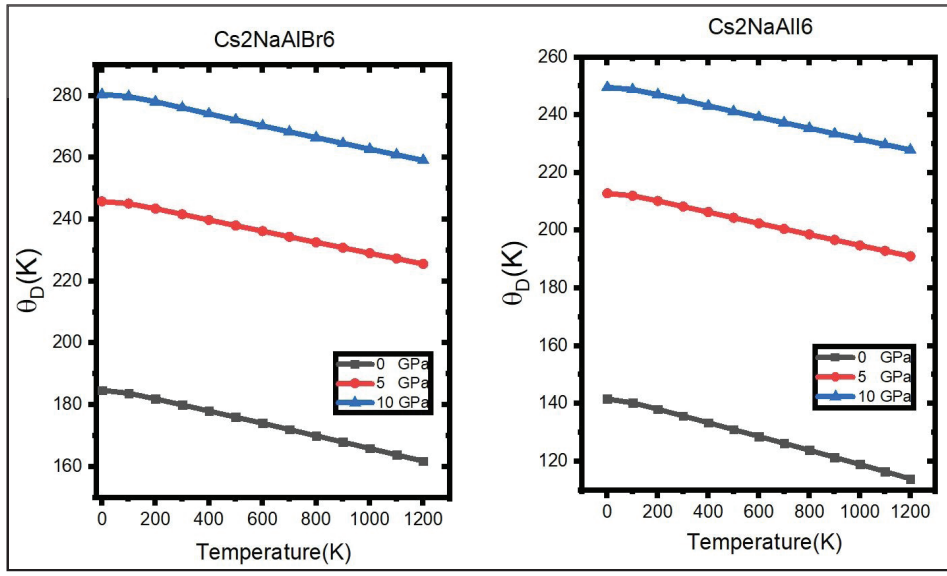

Fig. 14: Calculated Debye's Temperature of $Cs_2NaAl(Br/I)_6$.

Figure 14 illustrates our computed Debye temperature, a characteristic parameter delineating the average thermal vibrations of atoms or molecules within a crystal lattice. For $Cs_2NaAl(Br/I)_6$, the Debye temperature remains relatively constant within the range of 0 K to 100 K. This constancy arises from low anharmonicity and minimal expansion of the crystal structure with increasing temperature, leading to a nearly consistent Debye temperature. θ_D exhibits a gradual and nearly linear decrease as temperature rises, indicating alterations in the vibrational spectrum of atoms with changing temperature. Moreover, the Debye temperature can be used as a stand-in for measuring the hardness and strength of chemical bonds in a material; a higher Debye temperature corresponds to both stronger and harder bonds (Zelai *et al*. 2024). Accordingly, Figure 14 illustrates that the bond strength and hardness.

CONCLUSION

The novelty of this work lies in the comprehensive exploration of $Cs_2NaAl(Br/I)_6$ compounds, which are relatively uncharted in scientific research. By systematically investigating their structural, electronic, optical, and thermoelectric properties, this study provides the first detailed insights into their potential for advanced technological applications. These materials exhibit a unique combination of properties—thermodynamic stability, direct bandgaps, and high thermoelectric efficiency—that positions them as strong candidates for next-generation energy solutions. The ability to tune their electronic and optical behaviour through halogen substitution offers a versatile platform for optimizing performance in specific applications. For technological advancements, $Cs_2NaAl(Br/I)_6$ compounds could be implemented in efficient waste heat recovery systems, converting thermal energy into electricity with high efficiency. Their transparency and semiconductor-like properties make them suitable for optoelectronic devices, such as transparent conductors and photovoltaic cells, potentially leading to more efficient solar panels and energy-saving windows. Additionally, their stable cubic phase and mechanical robustness ensure durability in practical applications, making them reliable materials for long-term use in harsh environments.

Overall, the findings from this study not only introduce new materials with promising characteristics but also pave the way for their application in emerging technologies, contributing to the advancement of sustainable energy solutions and efficient electronic devices.

REFERENCES

Ali, M. A., Dar, S. A., AlObaid, A. A., Al-Muhimeed, T. I., Hegazy, H. H., Nazir, G., & Murtaza, G. (2021). Appealing perspectives of structural, electronic, mechanical, and thermoelectric properties of Tl2 (Se, Te) Cl6 vacancy-ordered double perovskites. *Journal of Physics and Chemistry of Solids*, *159*, 110258.

Ambrosch-Draxl, C., & Sofo, J. O. (2006). Linear optical properties of solids within the full-potential linearized augmented planewave method. *Computer physics communications*, *175*(1), 1-14.

Aravindan, V., Rajarajan, A. K., Vijayanarayanan, V., & Mahendran, M. (2022). First-principles calculations on novel Co-based equiatomic quaternary heusler alloys for spintronics. *Materials Science in Semiconductor Processing*, *150*, 106909.

Bartel, C. J., Sutton, C., Goldsmith, B. R., Ouyang, R., Musgrave, C. B., Ghiringhelli, L. M., & Scheffler, M. (2019). New tolerance factor to predict the stability of perovskite oxides and halides. *Science advances*, *5*(2), eaav0693.

Blaha, P., Schwarz, K., Madsen, G. K., Kvasnicka, D., & Luitz, J. (2001). wien2k. *An augmented plane wave+ local orbitals program for calculating crystal properties*, *60*(1).

Blancon, J. C., *et al*. (2020). First-Principles Calculations of Halide Perovskites: Methods, Accuracy, and Applications. *ACS Energy Letters*, 5(7), 1987-1996.

Cai, M. Q., Yin, Z., & Zhang, M. S. (2003). First-principles study of optical properties of barium titanate. *Applied physics letters*, *83*(14), 2805-2807.

Cai, Y., Xie, W., Teng, Y. T., Harikesh, P. C., Ghosh, B., Huck, P., ... & Asta, M. (2019). High-throughput computational study of halide double perovskite inorganic compounds. *Chemistry of Materials*, *31*(15), 5392-5401.

Chakraborty, S., Xie, W., Mathews, N., Sherburne, M., Ahuja, R., Asta, M., & Mhaisalkar, S. G. (2017). Rational design: A high-throughput computational screening and experimental validation methodology for lead-free and emergent hybrid perovskites. *ACS Energy Letters*, *2*(4), 837-845.

Charef, S., Assali, A., & Boukortt, A. (2024). Optoelectronic and thermoelectric properties of novel double halide perovskites Na2AgAsX6 (X= Cl, Br) for efficient green solar cells. *Materials Today Communications*, *38*, 108065.

Cheddadi, S., Boubendira, K., Meradji, H., Ghemid, S., Hassan, F. E. H., Lakel, S., & Khenata, R. (2017). First-principle calculations of structural, electronic, optical, elastic and thermal properties of MgXAs _ 2 MgXAs 2 (X= Si, Ge X= Si, Ge) compounds. *Pramana*, *89*, 1-10.

Gaillac, R., Pullumbi, P., & Coudert, F. X. (2016). ELATE: an open-source online application for analysis and visualization of elastic tensors. *Journal of Physics: Condensed Matter*, *28*(27), 275201.

Ghrib, T., Rached, A., Algrafy, E., Al-nauim, I. A., Albalawi, H., Ashiq, M. G. B., ... & Mahmood, Q. J. M. C. (2021). A new lead free double perovskites K2Ti (Cl/Br) 6; a promising materials for optoelectronic and transport properties; probed by DFT. *Materials Chemistry and Physics*, *264*, 124435.

Goldschmidt, V. M. (1926). Die gesetze der krystallochemie. *Naturwissenschaften*, *14*(21), 477-485.

Hnuna, L., & Pachuau, Z. (2023). Electronic, optical and thermoelectric properties of halide double perovskites Rb2AgInX6 (X= Cl, Br, I). *Physica Scripta*, *98*(3), 035814.

Huma, M., Rashid, M., Mahmood, Q., Algrafy, E., Kattan, N. A., Laref, A., & Bhatti, A. S. (2021). Physical properties of lead-free double perovskites A2SnI6 (A= Cs, Rb) using ab-initio calculations for solar cell applications. *Materials Science in Semiconductor Processing*, *121*, 105313.

Jain, A., Voznyy, O., Sargent, E. H., *et al*. (2018). Halide Perovskites and Their Emerging Applications. *Chemical Society Reviews*, 47(11), 3657-3672.

Jamal, M., Bilal, M., Ahmad, I., & Jalali-Asadabadi, S. (2018). IRelast package. *Journal of Alloys and Compounds*, *735*, 569-579.

Kale, A. J., Chaurasiya, R., & Dixit, A. (2021). Inorganic lead-Free Cs2AuBiCl6 perovskite absorber and Cu2O hole transport material based single-junction solar cells with 22.18% power conversion efficiency. *Advanced Theory and Simulations*, *4*(3), 2000224.

Kangsabanik, J., Sugathan, V., Yadav, A., Yella, A., & Alam, A. (2018). Double perovskites overtaking the single perovskites: A set of new solar harvesting materials with much higher stability and efficiency. *Physical Review Materials*, *2*(5), 055401.

Karim, M. M., Ganose, A. M., Pieters, L., Winnie Leung, W. W., Wade, J., Zhang, L., ... & Palgrave, R. G. (2019). Anion distribution, structural distortion, and symmetry-driven optical band gap bowing in mixed halide Cs2SnX6 vacancy ordered double perovskites. *Chemistry of materials*, *31*(22), 9430-9444.

Karki, B. B., Ackland, G. J., & Crain, J. (1997). Elastic instabilities in crystals from ab initio stress-strain relations. *Journal of Physics: Condensed Matter*, *9*(41), 8579.

Khandy, S. A., & Gupta, D. C. (2016). Structural, elastic and thermo-electronic properties of paramagnetic perovskite PbTaO 3. *RSC advances*, *6*(53), 48009-48015.

Kong, D., Cheng, D., Wang, X., Zhang, K., Wang, H., Liu, K., & Yin, L. (2020). Solution processed lead-free cesium titanium halide perovskites and their structural, thermal and optical characteristics. *Journal of Materials Chemistry C*, *8*(5), 1591-1597.

Kramers, H. A. (1927). The scattering of light by atoms Atti Cong. Intern. *Fisica (Transactions of Volta Centenary Congress) Como,* 2, 545–57.

Kronig, R. D. L. (1926). On the theory of dispersion of x-rays. *Josa*, *12*(6), 547-557.

Li, C., Lu, X., Ding, W., Feng, L., Gao, Y., & Guo, Z. (2008). Formability of abx3 (x= f, cl, br, i) halide perovskites. *Acta Crystallographica Section B: Structural Science*, *64*(6), 702-707.

M.A. Hadi, M. Roknuzzaman, A. Chroneos, A.K.M.A. Islam, R.V. Vovk, K. Ostrikov, S.H. Naqib, Elastic and thermodynamic properties of new $(Zr_{3-x}Ti_x)AlC2$ MAX-phase solid solutions, Comput. Mater. Sci. 137 (2017) 318e326.

Madsen, G. K., Carrete, J., & Verstraete, M. J. (2018). BoltzTraP2, a program for interpolating band structures and calculating semi-classical transport coefficients. *Computer Physics Communications*, *231*, 140-145.

Mahmood, Q., Younas, M., Ashiq, M. G. B., Ramay, S. M., Mahmood, A., & Ghaithan, H. M. (2021). First principle study of lead-free double perovskites halides Rb2Pd (Cl/Br) 6 for solar cells and renewable energy devices: a quantum DFT. *International Journal of Energy Research*, *45*(10), 14995-15004.

Murtaza, G., Alshahrani, T., Khalil, R. A., Mahmood, Q., Flemban, T. H., Althib, H., & Laref, A. (2021). Lead free double perovsites halides X2AgTlCl6 (X= Rb, Cs) for solar cells and renewable energy applications. *Journal of Solid State Chemistry*, *297*, 121988.

Nabi, M., & Gupta, D. C. (2021). Potential lead-free small band gap halide double perovskites Cs2CuMCl6 (M= Sb, Bi) for green technology. *Scientific reports*, *11*(1), 12945.

Noor, N. A., Mahmood, Q., Rashid, M., Haq, B. U., Laref, A., & Ahmad, S. A. (2018). Ab-initio study of thermodynamic stability, thermoelectric and optical properties of perovskites ATiO3 (A= Pb, Sn). *Journal of Solid State Chemistry*, *263*, 115-122.

Noor, N. A., Saddique, M. B., Haq, B. U., Laref, A., & Rashid, M. (2018). Investigations of half-metallic ferromagnetism and thermoelectric properties of cubic $XCrO_3$ (X= Ca, Sr, Ba) compounds via first-principles approaches. *Physics Letters A*, *382*(42-43), 3095-3102.

NREL (2020). A Comprehensive Review of Double Perovskites for Optoelectronic Applications. *Journal of Physical Chemistry Letters*, 11(15), 5963-5971.

Otero-de-la-Roza, A., Abbasi-Pérez, D., & Luaña, V. (2011). Gibbs2: A new version of the quasiharmonic model code. II. Models for solid-state thermodynamics, features and implementation. *Computer Physics Communications*, *182*(10), 2232-2248.

Pan, R. K., Wang, H. C., Shi, T. T., Tian, X., & Tang, B. Y. (2016). Thermal properties and thermoelasticity of L12 ordered Al_3RE (RE= Er, Tm, Yb, Lu) phases: a first-principles study. *Materials & Design*, *102*, 100-105.

Penn, D. R. (1962).Wave number dependent dielectric function of semiconductors. *Physical Review*, *128*(5), 2093

Reshak, A. H., Fedorchuk, A. O., Lakshminarayana, G., Alahmed, Z. A., Kamarudin, H., & Auluck, S. (2013). Influence of different exchange correlation potentials on band structure and optical constant calculations of ZrGa2 and ZrGe2 single crystals. *Computational materials science*, *78*, 134-139.

Saeed, Y., Amin, B., Khalil, H., Rehman, F., Ali, H., Khan, M. I., ... & Shafiq, M. (2020). Cs 2 NaGaBr 6: a new lead-free and direct band gap halide double perovskite. *RSC advances*, *10*(30), 17444-17451.

Slavney, A. H., Hu, T., Lindenberg, A. M., & Karunadasa, H. I. (2016). A bismuth-halide double perovskite with long carrier recombination lifetime for photovoltaic applications. *Journal of the American chemical society*, *138*(7), 2138-2141.

Takeuchi, T. (2009). Conditions of electronic structure to obtain large dimensionless figure of merit for developing practical thermoelectric materials. *Materials transactions*, *50*(10), 2359-2365.

Tran, F., & Blaha, P. (2009). Accurate band gaps of semiconductors and insulators with a semilocal exchange-correlation potential. *Physical review letters*, *102*(22), 226401.

Tritt, T. M., & Rowe, D. (2005). Thermoelectrics handbook: macro to nano. *Thermoelectrics Handbook: Macro to Nano*.

Volonakis, G., Haghighirad, A. A., Milot, R. L., Sio, W. H., Filip, M. R., Wenger, B., ... & Giustino, F. (2017). Cs2InAgCl6: a new lead-free halide double perovskite with direct band gap. *The journal of physical chemistry letters*, *8*(4), 772-778.

Yang, J., Qiu, P., Liu, R., Xi, L., Zheng, S., Zhang, W., & Yang, J. (2011). Trends in electrical transport of p-type skutterudites R Fe_4 Sb_{12} (R= Na, K, Ca, Sr, Ba, La, Ce, Pr, Yb) from first-principles calculations and Boltzmann transport theory. *Physical Review B*, *84*(23), 235205.

Yousuf, S., & Gupta, D. C. (2017). Investigation of electronic, magnetic and thermoelectric properties of Zr_2NiZ (Z= Al, Ga) ferromagnets. *Materials Chemistry and Physics*, *192*, 33-40.

Zelai, T., Mustafa, G. M., Alotaibi, S., Younas, B., Alhajri, F., Saba, S., ... & Mahmood, Q. (2024). Study of electronic, mechanical, thermoelectric, and optical aspects of K2AlAg (Br/I) 6 for solar cells, and energy storage applications. *Inorganic Chemistry Communications*, *163*, 112344.

Zhang, Y., Li, L., Bai, W., Shen, B., Zhai, J., & Li, B. (2015). Effect of CaZrO 3 on phase structure and electrical properties of KNN-based lead-free ceramics. *RSC Advances*, *5*(25), 19647-19651.

Zhao, L. D., Tan, G., & Kanatzidis, M. G. (2016). Thermoelectric Performance of Halide Perovskites. *Nature Reviews Materials*, 1(10), 16075.

Ziane, M. I., Bensaad, Z., Labdelli, B., & Bennacer, H. (2014). First-principles study of structural, electronic and optical properties of III-arsenide binary GaAs and InAs, and III-nitrides binary GaN and InN: Improved density-functional-theory Study. *Sensors & transducers, 27*(5), 374.